Ultrasonics 94 (2019) 419–429

Contents lists available at ScienceDirect

Ultrasonics

journal homepage: www.elsevier.com/locate/ultras

Maximizing wave attenuation in viscoelastic phononic crystals by topology optimization

Yafeng Chen[a], Di Guo[a], Yang Fan Li[b], Guangyao Li[a,c], Xiaodong Huang[b,a,*]

[a] Key Laboratory of Advanced Technology for Vehicle Body Design & Manufacture, Hunan University, Changsha 410082, China
[b] Faculty of Science, Engineering and Technology, Swinburne University of Technology, Hawthorn, VIC 3122, Australia
[c] Collaborative Innovation Center of Intelligent New Energy Vehicle, Shanghai 200092, China

ARTICLE INFO

Keywords:
Viscoelastic composite
Phononic crystals
Wave attenuation
Bi-directional evolutionary structural optimization (BESO)

ABSTRACT

The viscoelasticity of constituent materials has a significant effect on the dispersion relation of waves in viscoelastic phononic crystals (PCs). This paper extends the bi-directional evolutionary structure optimization (BESO) method to the design of viscoelastic PCs with the maximum attenuation and stiffness. The attenuation factor is calculated by the $\mathbf{k}(\omega)$-method, and the effective elasticity matrix of composite PCs is extracted by the homogenization theory. The inverse design of viscoelastic PCs is formulated with a topology optimization problem, which is then solved by the proposed BESO method. Generally, BESO re-distributes the material phases of viscoelastic PCs within the primitive unit cell step by step based on sensitivity analysis. The optimization process is stopped until the optimized viscoelastic PC with the maximum attenuation factor and the desirable bulk modulus is achieved. Numerical examples are systematically presented for the propagation of out-of-plane or in-plane waves, and combined out-of-plane and in-plane waves at various frequencies. Novel topological patterns of the optimized viscoelastic PCs are obtained and discussed.

1. Introduction

Elastic phononic crystals (PCs) are usually artificial composites made of periodically distributed material phases with high contrast in density and elastic constants [1]. The phononic band gap is a frequency range, within which the propagation of mechanical waves is prohibited, and only evanescent waves with spatial decay are allowed. PCs with band gaps have a wide range of potential applications in sound insulation [2–5], defect based energy trapping [6–9], acoustic filtering [10–12], and waveguiding [13–18].

Numerous studies have explored the properties of PCs with linear elastic constituents, where the wave dissipation can be neglected. However, most of the realistic materials such as rubber and epoxy, which are widely used as components of PCs, exhibit viscoelastic behaviors [19]. The presence of the viscosity factor naturally leads to temporal damping or spatial attenuation of waves in viscoelastic PCs, and further changes the band structure and transmission spectra. The effect of the viscoelasticity on wave dispersion has been studied in recent years. For example, Ba'Ba'AHA and Nouh investigated the vibrational power flow in one-dimensional dissipative phononic structures [20]. Frazier and Hussein presented the dispersion analysis for complex frequencies and wavenumbers of phononic crystals and metamaterials [21,22]. Ma et al. investigated the mechanical performance of a damper with metal rubber particles distributed in an auxetic cellular configuration [23]. Moiseyenko and Laude [24] studied the influence of the viscosity of materials, which increases linearly with frequency, on the complex band structure of two-dimensional viscoelastic PCs. Laude et al. [25] theoretically analyzed the effect of loss on the dispersion relation of waves in viscoelastic PCs and photonic crystals. Oh et al. [26] investigated the wave attenuation and dissipation mechanism in viscoelastic PCs with different inclusions for the long-wavelength regime. Manimala and Sun [27] studied the stress wave attenuation of locally dissipative acoustic metamaterials with various microstructures of damped oscillators. Wang et al. [28] and Krushynska et al. [29] discussed the wave attenuation of locally resonant viscoelastic PCs. They found that the viscoelastic damping of constituent materials decreases the attenuation performance within phononic band gaps, but improves the attenuation bandwidth on the other hand.

The methods to analyze the dynamic behavior of viscoelastic PCs can be divided into two groups, the $\omega(\mathbf{k})$- and $\mathbf{k}(\omega)$-approaches [30,31]. The $\omega(\mathbf{k})$-approach deals with real-valued wave vectors of free wave propagation and complex-valued frequencies, i.e. $\omega = \omega' + i\omega''$, where the imaginary part ω'' measures the damping of the corresponding mode [32–35]. Neverthelss, the $\mathbf{k}(\omega)$-approach deals with real-valued

* Corresponding author at: Faculty of Science, Engineering and Technology, Swinburne University of Technology, Hawthorn, VIC 3122, Australia.
E-mail address: xhuang@swin.edu.au (X. Huang).

https://doi.org/10.1016/j.ultras.2018.05.005
Received 23 October 2017; Received in revised form 13 May 2018; Accepted 14 May 2018
Available online 17 May 2018
0041-624X/

frequencies of harmonic wave propagation and complex-valued wave vectors, i.e. $k = k' + ik''$, where the imaginary k'' describes the wave attenuation [24,28,30,36]. In this paper, the matrix material of PCs is assumed to be viscoelastic, and its mechanical property is a function of frequency. It is easier to solve this nonlinear problem by setting the frequency as an input parameter rather than an output of the dispersion analysis. Therefore, the $\mathbf{k}(\omega)$-approach will be used in this study and the minimum imaginary k'' at a specific frequency will be selected as the attenuation factor [26,28,37].

Since the physical properties of PCs highly depend on the spatial distribution of the constituent materials, topological design of PCs has attracted growing attention in recent years [38]. Sigmund and Jensen [39] first conducted the optimization of phononic band gap crystals by combining finite element method (FEM) with the method of moving asymptotes (MMA). After that, genetic algorithm (GA) or gradient-based topology optimization technique, in conjunction with the fast plane wave expansion method (FPWE) or FEM, were developed to maximize the relative or absolute band gap width of elastic PCs [40–46]. Li et al. [47,48] extended the bi-directional evolutionary structural optimization (BESO) method for maximizing band gaps of in-plane and out-of-plane elastic waves. Alessandro et al. [49] used BESO for shape optimization of porous elastic PC slabs with widest full 3D bandgap. Chen et al. [50] maximized the spatial decay of evanescent waves in elastic PCs using BESO. Huang et al. [51] performed topology optimization of composite microstructures with the desirable viscoelastic characteristics. Andreassen et al. [52] conducted topology optimization of viscoelastic PCs for maximizing the attenuation of in-plane waves by assuming constant loss factors of the constituents. However, the wave attenuation by viscoelastic materials is dependent on the operation frequency. And the traditional band structure that plots $\omega(\boldsymbol{k})$ is also unsuitable for viscoelastic PCs due to the non-existence of purely real wavefunction except for waves at a low-frequency range.

Since most realistic phononic crystals are dispersive and have losses, topology optimization of a PC should also consider its dispersive and dissipative effects. In this paper, we will investigate topology optimization of 2D viscoelastic PCs for maximizing the minimum attenuation of waves propagating in all possible directions, which has never been explored before. Meanwhile, the stiffness of viscoelastic PCs will be considered as the constraint function so that the resulting viscoelastic PCs enable to sustain a certain amount of static loading. The rest of the paper is organized as follows. Section 2 introduces the $\mathbf{k}(\omega)$ approach for calculating the complex band diagram and the homogenization theory for extracting the effective bulk modulus. Then the optimization problem is mathematically formulated, and elemental sensitivities are derived. Numerical implementation of the BESO method for optimizing viscoelastic PCs is described in Section 3. Section 4 presents various examples of optimized viscoelastic PCs for the propagation of out-of-plane and in-plane evanescent waves and the combined out-of-plane and in-plane evanescent waves. The conclusions are drawn in Section 5.

2. Theory and optimization problem

2.1. Analysis of waves in viscoelastic phononic crystals

When elastic waves propagate in PCs, the governing equation can be expressed as follows

$$\rho(\mathbf{r})\ddot{\mathbf{u}} = \nabla[\lambda^*(\mathbf{r}) + 2\mu^*(\mathbf{r})](\nabla\mathbf{u}) - \nabla\times[\mu^*(\mathbf{r})\nabla\times\mathbf{u}] \tag{1}$$

where λ^* and μ^* are complex Lame's coefficients, ρ is the material density and $\mathbf{u} = (u_x, u_y, u_z)$ is the displacement vector. For 2D PCs, $\mathbf{r}(x, y)$ denotes the position vector and the wave fields are independent of z, i.e. $\partial\mathbf{u}/\partial z = 0$. Thus, Eq. (1) can be decoupled into the mixed in-plane waves and out-of-plane shear waves:

$$\rho(\mathbf{r})\frac{\partial^2 u_x}{\partial t^2} = \frac{\partial}{\partial x}\left[(\lambda^*(\mathbf{r}) + 2\mu^*(\mathbf{r}))\frac{\partial u_x}{\partial x} + \lambda^*(\mathbf{r})\frac{\partial u_y}{\partial y}\right] + \frac{\partial}{\partial y}\left[\mu^*(\mathbf{r})\left(\frac{\partial u_x}{\partial y} + \frac{\partial u_y}{\partial x}\right)\right] \tag{2}$$

$$\rho(\mathbf{r})\frac{\partial^2 u_y}{\partial t^2} = \frac{\partial}{\partial x}\left[\mu^*(\mathbf{r})\left(\frac{\partial u_x}{\partial y} + \frac{\partial u_y}{\partial x}\right)\right] + \frac{\partial}{\partial y}\left[\lambda^*(\mathbf{r})\frac{\partial u_x}{\partial x} + (\lambda^*(\mathbf{r}) + 2\mu^*(\mathbf{r}))\frac{\partial u_y}{\partial y}\right] \tag{3}$$

$$\rho(\mathbf{r})\frac{\partial^2 u_z}{\partial t^2} = \frac{\partial}{\partial x}\left[\mu^*(\mathbf{r})\frac{\partial u_z}{\partial x}\right] + \frac{\partial}{\partial y}\left[\mu^*(\mathbf{r})\frac{\partial u_z}{\partial y}\right] \tag{4}$$

Due to the periodicity of PCs, the displacement vector $\mathbf{u}(\mathbf{r})$ can be expressed by the Bloch wave expansion as,

$$\mathbf{u}(\mathbf{r},\mathbf{k}) = \mathbf{u}_k(\mathbf{r})e^{i(\omega t + \mathbf{k}\cdot\mathbf{r})} \tag{5}$$

where $\mathbf{u}_k(\mathbf{r})$ is a periodic function of $\mathbf{r}$ with the same periodicity of the structure; $\mathbf{k} = (k_x, k_y)$ is the Bloch wave vector [53]; $\lambda^*(\mathbf{r}) = \lambda^*(\mathbf{r} + \mathbf{a})$ and $\mu^*(\mathbf{r}) = \mu^*(\mathbf{r} + \mathbf{a})$, where the square lattice $\mathbf{a} = (a, a)$. With the periodic boundary conditions, it is sufficient to solve the governing equations in the primitive unit cell, as shown in Fig. 1(a). By substituting Eq. (5) into either Eqs. (2) and (3) or Eq. (4), the governing equations can be converted to two eigenvalue problems for in-plane waves and out-of-plane waves, respectively. When the viscosity of the constituents is considered, all the waves become evanescent [28,29]. To identify the characteristics of evanescent waves, it is necessary to apply the $\mathbf{k}(\omega)$ method to solve the resulting eigenvalue equations by sweeping frequency.

Let $k_x = k\cos\theta$ and $k_y = k\sin\theta$, where θ is the incident angle of the wave as illustrated in Fig. 1(b). When the primitive unit cell is discretized with finite elements, the eigenvalue problems can thus be written as,

$$(k^2\mathbf{K}_\mathrm{I}^* + k\mathbf{K}_\mathrm{II}^* + \mathbf{K}_\mathrm{III}^*)\mathbf{u} = \mathbf{0} \tag{6}$$

where $\mathbf{u} = \mathbf{u}_k(\mathbf{r})$ is the Bloch nodal displacement. According to the elastic-viscoelastic correspondence principle for harmonic waves, the matrices $\mathbf{K}_\mathrm{I}^*$, $\mathbf{K}_\mathrm{II}^*$, $\mathbf{K}_\mathrm{III}^*$ can be obtained by replacing the corresponding elastic material parameters of $\mathbf{K}_\mathrm{I}$, $\mathbf{K}_\mathrm{II}$, $\mathbf{K}_\mathrm{III}$ in Ref. [50] with the viscoelastic ones in this paper.

Note that Eq. (6) is a quadratic equation involving unknown wavenumbers, which is hard to be solved directly. It needs to be rewritten in the standard form of an eigenvalue problem as,

$$(\mathbf{K}(\theta,\omega) - k\mathbf{M}(\theta))\overline{\mathbf{U}} = \mathbf{0} \tag{7}$$

where

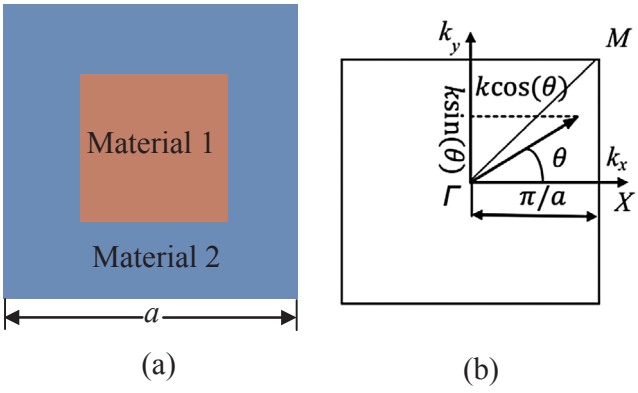

Fig. 1. (a) The primitive unit cell of a typical viscoelastic PC with two phases, where a is the lattice constant; (b) Illustration of the propagation direction specified by the angle θ and the irreducible first Brillouin zone (Γ-X-M-Γ).

$$\mathbf{K} = \begin{bmatrix} \mathbf{K}_{\mathrm{II}}^{*} & \mathbf{K}_{\mathrm{III}}^{*} \\ \mathrm{I} & \mathbf{0} \end{bmatrix}, \mathbf{M} = \begin{bmatrix} -\mathbf{K}_{\mathrm{I}}^{*} & \mathbf{0} \\ \mathbf{0} & \mathrm{I} \end{bmatrix}, \overline{\mathbf{U}} = \begin{bmatrix} k\mathbf{u} \\ \mathbf{u} \end{bmatrix}$$

For a given frequency ω and angle θ, Eq. (7) can be solved for corresponding eigenvalues, k. The wave vector k for viscoelastic PCs is a complex value taking the form, $k = k' + ik''$. The attenuation factor is defined by the minimum of the positive imaginary part of k in all possible directions [26,28,37], and is selected as the optimization objective in this study.

Similar to the design of phononic band gap crystals [47,48], the design of viscoelastic PCs in this paper is also restricted with 45° symmetry. Due to the symmetry, only waves propagating along the direction within the irreducible first Brillouin zone need to be considered, as denoted in Fig. 1(b) and $\theta \in [0°, 45°]$. We choose ten equally divided directions between 0° and 45° as a result of the compromise between the computational cost and the accuracy of solutions.

2.2. Effective stiffness of viscoelastic PCs

In the real applications, a viscoelastic PC should possess a certain stiffness to sustain possible external loadings. Due to the periodic nature of the PC, its effective elasticity matrix under static condition can be calculated by homogenization theory [54,55] which is expressed by

$$E_{lm}^{H} = \frac{1}{|Y|}\int_{\Omega} (\{\varepsilon_0^l\} - \{\varepsilon^l\})^T [E] (\{\varepsilon_0^m\} - \{\varepsilon^m\}) d\Omega \tag{8}$$

where E_{lm}^{H} is the homogenized elasticity matrix of the viscoelastic PC and the subscripts l,m = 1,2,3 for 2D viscoelastic PCs. $[E]$ is the elasticity matrix of the constituent at a given position within the unit cell, i.e., the domain Ω. $|Y|$ denotes the area of the unit cell. $\{\varepsilon_0^l\}$ denotes the three linear independent test strain fields, e.g., $\{\varepsilon_0^1\} = \{1,0,0\}$, $\{\varepsilon_0^2\} = \{0,1,0\}$, $\{\varepsilon_0^3\} = \{0,0,1\}$. $\{\varepsilon^l\}$ is the resulting strain field induced by the corresponding test strain, $\{\varepsilon_0^l\}$. The stiffness of the viscoelastic PCs is characterized by the homogenized bulk modulus κ^H, which can be expressed by the components of the effective elasticity matrix

$$\kappa^H = \frac{1}{4}(E_{11}^H + E_{12}^H + E_{21}^H + E_{22}^H) \tag{9}$$

It is desirable to maximize the attenuation factor and the bulk modulus simultaneously using the weighting scheme or maximize the attenuation factor under a specified bulk modulus, κ^*. Here, we attack the later one so that the resulting viscoelastic PCs can possess an excellent attenuation property while satisfying a given stiffness constraint. To assign the constraint value properly, it is necessary to explore the achievable value of the bulk modulus for a given viscoelastic PC.

For a two-phase viscoelastic PC composed of material 1 and material 2, the maximum bulk modulus can be estimated according to the Hashin-Shtrikman (HS) bounds [56]. Under a given volume fraction of material 2, V_f^2, the upper bound of the bulk modulus can be calculated by

$$\kappa_{upper} = \kappa_2 + \frac{1 - V_f^2}{\frac{1}{\kappa_1 - \kappa_2} + \frac{3V_f^2}{3\kappa_2 + 4G_2}} \tag{10}$$

where κ_1 and κ_2 are the bulk modulus of material 1 and material 2, respectively, and $\kappa_2 > \kappa_1$. G_2 is the shear modulus of material 2.

Therefore, the stiffness constraint, κ^*, in our optimization problem should not be greater than κ_{upper}. Otherwise $\kappa^H \geqslant \kappa^*$ can never be satisfied. The selection of the stiffness constraint κ^* will be discussed in the numerical examples.

2.3. Topology optimization formulations

Our optimization aims to maximize the attenuation factor of waves at a specified frequency by viscoelastic PCs subjected to given material volume and homogenized stiffness. The attenuation factor is measured by the minimum of the imaginary part of wave vectors, k_θ''. To maximize the minimum attenuation of waves propagating in all possible directions, the smallest k_θ'' in all calculated angles is selected as the objective function. After the discretization of the primitive unit cell, an artificial design variable, x_i (i = 1, 2, …,n), will be assigned to each element, where x_i = 0 or 1. It is assumed that the viscoelastic PCs are constructed by two isotropic solids, material 1 and material 2. x_i = 0 denotes element i is composed of material 1 while x_i = 1 for material 2. Thus, the optimization problem can be mathematically formulated as follows

$$\begin{cases} \max: & f(x_i) = \min(k_{\theta_j}'') \\ \text{st.}: & \kappa^H \geqslant \kappa^* = \beta\kappa_{upper} \\ & V_f^2 = V_f^* \\ & \theta_j = [0°{:}\ 5°{:}\ 45°]\,; j = 1, 2, \cdots, 10 \\ & x_i = 0 \text{ or } 1;\ i = 1, 2, \cdots, n \end{cases} \tag{11}$$

where k_{θ_j}'' denotes the minimum of the imaginary part of wave vectors at angle θ_j. V_f^2 denotes the volume fraction of material 2 in the primitive unit cell and V_f^* is the prescribed volume of material 2. β is the ratio between the stiffness constraint and the corresponding upper bound at the volume V_f^2. Obviously, the value of β is between 0 and 1.

To obtain the gradient information of the objective function with respect to the design variables, it is necessary to interpolate the material properties between these of two materials. The linear material interpolation scheme has been applied successfully in the optimization of maximizing spatial decay of evanescent waves in elastic PCs [50] and is adopted here

$$\rho(x_i) = (1 - x_i)\rho_1 + x_i\rho_2 \tag{12}$$

$$\lambda^*(x_i) = (1 - x_i)\lambda_1^* + x_i\lambda_2^* \tag{13}$$

$$\mu^*(x_i) = (1 - x_i)\mu_1^* + x_i\mu_2^* \tag{14}$$

where subscripts '1' and '2' represent the properties in materials 1 and 2, respectively. The well-ordered properties of two constituent materials are assumed e.g. $\rho_2 > \rho_1$, $\mathrm{real}(\lambda_2^*) > \mathrm{real}(\lambda_1^*)$, and $\mathrm{real}(\mu_2^*) > \mathrm{real}(\mu_1^*)$.

However, the well-known solid isotropic material penalization (SIMP) model [55] is used in the calculation of the homogenized stiffness.

$$\boldsymbol{E}(x_i) = \boldsymbol{E}_1(1 - x_i^p) + \boldsymbol{E}_2 x_i^p \tag{15}$$

where E1 and E2 are constitutive matrix for material phases 1 and 2 respectively. The penalty exponent p > 1 is artificially chosen to ensure that the solution would converge to a clear 0/1 design.

The sensitivity of the objective function with respect to design variable x_i can be written as,

$$\frac{\partial f(x_i)}{\partial x_i} = \frac{\partial \min(k_{\theta_j}'')}{\partial x_i} \tag{16}$$

Differentiating both sides of Eq. (6) with respect to x_i yields the following equation,

$$\begin{aligned} \frac{\partial((k^2\mathbf{K}_{\mathrm{I}}^* + k\mathbf{K}_{\mathrm{II}}^* + \mathbf{K}_{\mathrm{III}}^*)\mathbf{u})}{\partial x_i} &= \frac{\partial k}{\partial x_i}(2k\mathbf{K}_{\mathrm{I}}^*\mathbf{u} + \mathbf{K}_{\mathrm{II}}^*\mathbf{u}) \\ &+ \left(k^2\frac{\partial \mathbf{K}_{\mathrm{I}}^*}{\partial x_i} + k\frac{\partial \mathbf{K}_{\mathrm{II}}^*}{\partial x_i} + \frac{\partial \mathbf{K}_{\mathrm{III}}^*}{\partial x_i}\right)\mathbf{u} \\ &+ (k^2\mathbf{K}_{\mathrm{I}}^* + k\mathbf{K}_{\mathrm{II}}^* + \mathbf{K}_{\mathrm{III}}^*)\frac{\partial \mathbf{u}}{\partial x_i} = 0 \end{aligned} \tag{17}$$

Multiplying both sides of Eq. (17) with a vector, $\mathbf{v}^T$ gets,

$$\frac{\partial k}{\partial x_i}(2k\mathbf{v}^T\mathbf{K}_{\mathrm{I}}^*\mathbf{u}+\mathbf{v}^T\mathbf{K}_{\mathrm{II}}^*\mathbf{u})+\mathbf{v}^T\left(k^2\frac{\partial \mathbf{K}_{\mathrm{I}}^*}{\partial x_i}+k\frac{\partial \mathbf{K}_{\mathrm{II}}^*}{\partial x_i}+\frac{\partial \mathbf{K}_{\mathrm{III}}^*}{\partial x_i}\right)\mathbf{u} + \mathbf{v}^T(k^2\mathbf{K}_{\mathrm{I}}^*+k\mathbf{K}_{\mathrm{II}}^*+\mathbf{K}_{\mathrm{III}}^*)\frac{\partial \mathbf{u}}{\partial x_i}=0 \tag{18}$$

To eliminate the unknown $\frac{\partial \mathbf{u}}{\partial x_i}$ from the above equation, $\mathbf{v}^T$ is chosen such that

$$\mathbf{v}^T(k^2\mathbf{K}_{\mathrm{I}}^*+k\mathbf{K}_{\mathrm{II}}^*+\mathbf{K}_{\mathrm{III}}^*)=0 \quad \text{or}(k^2\mathbf{K}_{\mathrm{I}}^*+k\mathbf{K}_{\mathrm{II}}^*+\mathbf{K}_{\mathrm{III}}^*)^T\mathbf{v}=0 \tag{19}$$

Eq. (19) denotes the adjoint equation and $\mathbf{v}$ denotes eigenvectors. It should be noted that the adjoint equation is different from the original eigenvalue problem in Eq. (6) since the matrix $\mathbf{K}_{\mathrm{I}}^*$, $\mathbf{K}_{\mathrm{II}}^*$ and $\mathbf{K}_{\mathrm{III}}^*$ are non-symmetric. To this end, the sensitivity of a wave vector with respect to x_i is calculated by

$$\frac{\partial k}{\partial x_i}=-\frac{\mathbf{v}^T\left(k^2\frac{\partial \mathbf{K}_{\mathrm{I}}^*}{\partial x_i}+k\frac{\partial \mathbf{K}_{\mathrm{II}}^*}{\partial x_i}+\frac{\partial \mathbf{K}_{\mathrm{III}}^*}{\partial x_i}\right)\mathbf{u}}{2k\mathbf{v}^T\mathbf{K}_{\mathrm{I}}^*\mathbf{u}+\mathbf{v}^T\mathbf{K}_{\mathrm{II}}^*\mathbf{u}} \tag{20}$$

And

$$\frac{\partial k''}{\partial x_i}=\mathrm{imag}\left(\frac{\partial k}{\partial x_i}\right) \tag{21}$$

The derivatives of the matrices $\frac{\partial \mathbf{K}_{\mathrm{I}}^*}{\partial x_i}$, $\frac{\partial \mathbf{K}_{\mathrm{II}}^*}{\partial x_i}$, $\frac{\partial \mathbf{K}_{\mathrm{III}}^*}{\partial x_i}$ can be obtained by replacing the corresponding elastic material parameters of $\frac{\partial \mathbf{K}_{\mathrm{I}}}{\partial x_i}$, $\frac{\partial \mathbf{K}_{\mathrm{II}}}{\partial x_i}$, $\frac{\partial \mathbf{K}_{\mathrm{III}}}{\partial x_i}$ in Ref. [50] with the viscoelastic ones in this paper.

Similarly, the sensitivity of the constraint function with respect to a design variable can be formulated as,

$$\frac{\partial \kappa^H}{\partial x_i}=\frac{1}{4}\left(\frac{\partial E_{11}^H}{\partial x_i}+\frac{\partial E_{12}^H}{\partial x_i}+\frac{\partial E_{21}^H}{\partial x_i}+\frac{\partial E_{22}^H}{\partial x_i}\right) \tag{22}$$

Using the adjoint variable method [57], the derivative of the homogenized elasticity matrix can be calculated by,

$$\frac{\partial E_{lm}^H}{\partial x_i}=\frac{1}{|Y|}\int_\Omega(\{\varepsilon_0^l\}-\{\varepsilon^l\})^T\frac{\partial E_{lm}}{\partial x_i}(\{\varepsilon_0^m\}-\{\varepsilon^m\})d\Omega \tag{23}$$

Considering the material interpolation scheme in Eq. (15), the sensitivity of the homogenized elasticity matrix can be written as,

$$\frac{\partial E_{lm}^H}{\partial x_i}=\frac{px_i^{p-1}}{|Y|}\int_\Omega(\{\varepsilon_0^l\}-\{\varepsilon^l\})^T(E_{lm}^2-E_{lm}^1)(\{\varepsilon_0^m\}-\{\varepsilon^m\})d\Omega \tag{24}$$

where E_{lm}^1 and E_{lm}^2 are the elasticity matrix of material 1 and material 2, respectively.

3. Numerical implementation and BESO procedure

3.1. Modification of the objective function

The objective function given in Eq. (11) is a complicate max-min problem and the location of $\min(k_{\theta_j}'')$ often varies with the change of topology of the primitive unit cell. This may cause the instability of the optimization process. To avoid this problem, we introduce a bound C_1 in the vicinity of $\min(k_{\theta_j}'')$ and C_1 is defined by,

$$C_1=1.1\min(k_{\theta_j}'') \tag{25}$$

Thus, all the imaginary parts of wave vectors between $[\min(k_{\theta_j}''), C_1]$ will be considered in the optimization and the objective function is modified to,

$$\overline{f}(x_i)=\sum_{j=1}^{N}w_jk_{\theta_j}'' \tag{26}$$

where N represents the number of directions of wave vectors. w_j is the weight factor as,

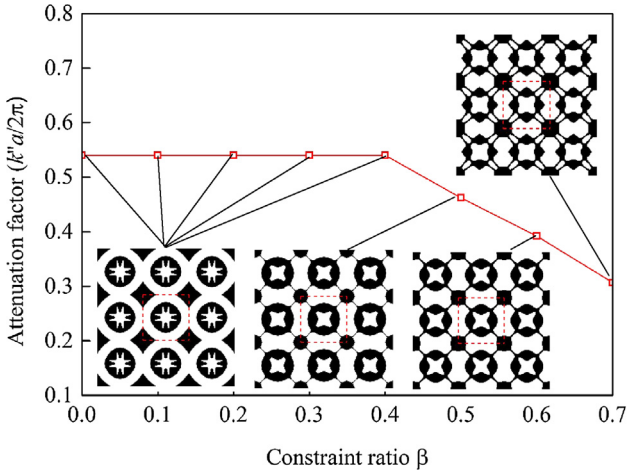

Fig. 2. Optimized attenuation factors against different constraint ratios and the corresponding topologies.

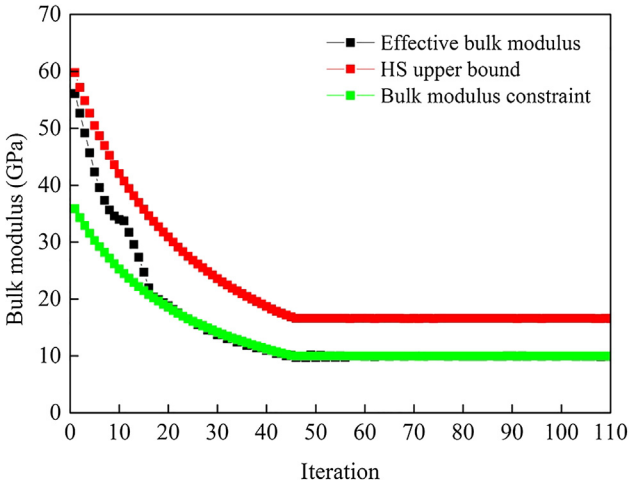

Fig. 3. Evolution histories of the effective bulk modulus, bulk modulus constraint and the corresponding HS upper bound for the optimization case with $\Omega = 0.9$ and $\beta = 0.6$.

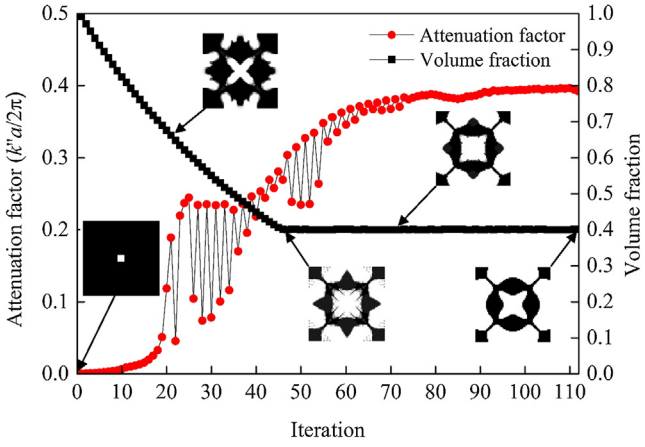

Fig. 4. Evolution histories of attenuation factor, volume fraction and topology of primitive unit cell for the optimization case with $\Omega = 0.9$ and $\beta = 0.6$.

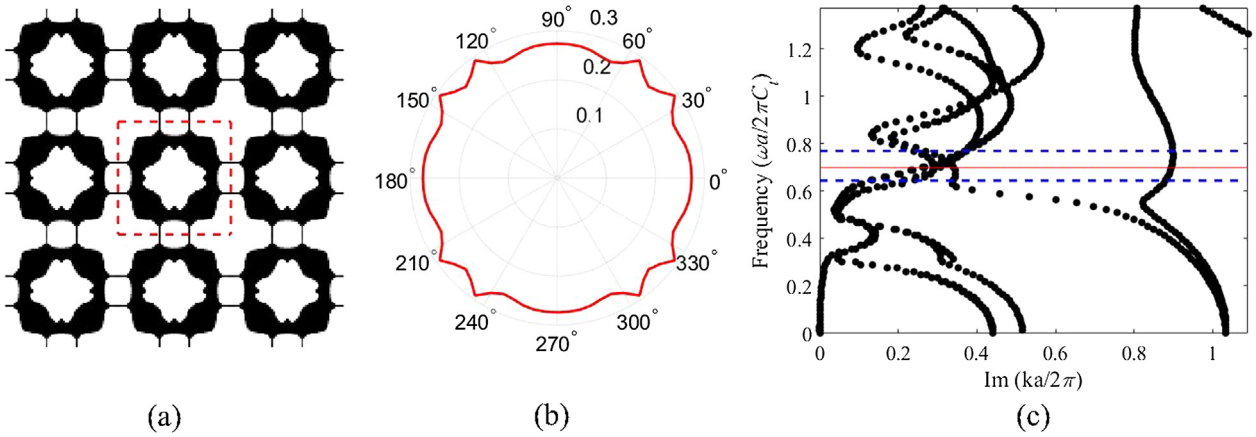

Fig. 5. (a) Optimized topology, (b) equal attenuation factor contour and (c) the imaginary part of complex band diagram (the blue dotted lines denote upper and bottom bounds of the band gap, the red solid line denote the specified frequency) for $\theta = 25°$ for out-of-plane waves at frequency $\Omega = 0.7$. (For interpretation of the references to colour in this figure legend, the reader is referred to the web version of this article.)

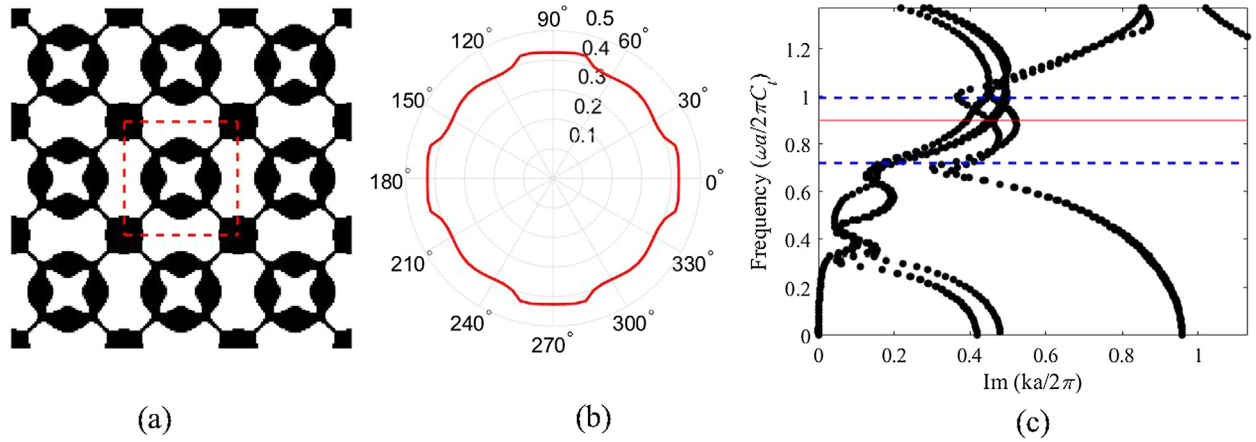

Fig. 6. (a) Optimized topology, (b) equal attenuation factor contour and (c) the imaginary part of complex band diagram for $\theta = 25°$ for out-of-plane waves at frequency $\Omega = 0.9$.

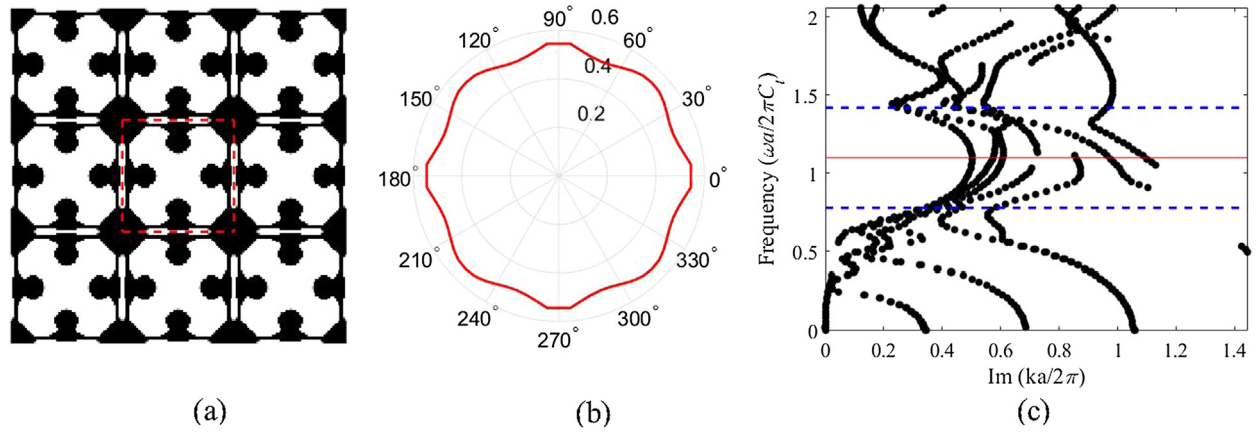

Fig. 7. (a) Optimized topology, (b) equal attenuation factor contour and (c) the imaginary part of complex band diagram for $\theta = 20°$ for out-of-plane waves at frequency $\Omega = 1.1$.

$$w_j = \frac{A_j}{\sum_{j=1}^{N} A_j} \tag{27}$$

where A_j is defined by,

$$A_j = \begin{cases} C_1 - \min(k''_{\theta_j}) & \text{when} \quad k''_{\theta_j} < C_1 \\ 0 & \text{when} \quad k''_{\theta_j} > C_1 \end{cases} \tag{28}$$

As a result, $\sum_{j=1}^{N} w_j = 1$.

The current optimization problem stated in Eq. (11) has multiple constraints, including a volume constraint and a stiffness constraint. In the BESO method, the volume constraint can be easily implemented

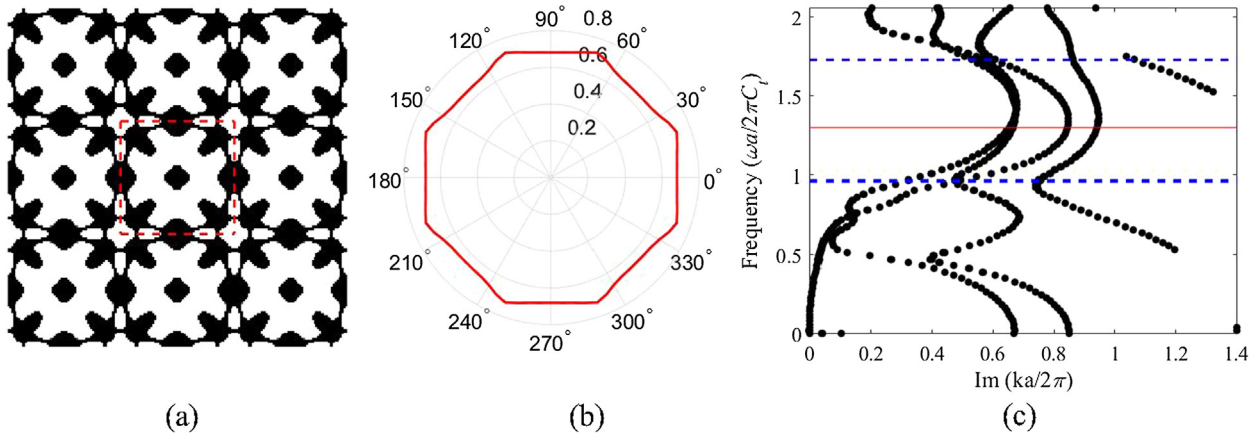

Fig. 8. (a) Optimized topology, (b) equal attenuation factor contour and (c) the imaginary part of complex band diagram for $\theta = 45°$ for out-of-plane waves at frequency $\Omega = 1.3$.

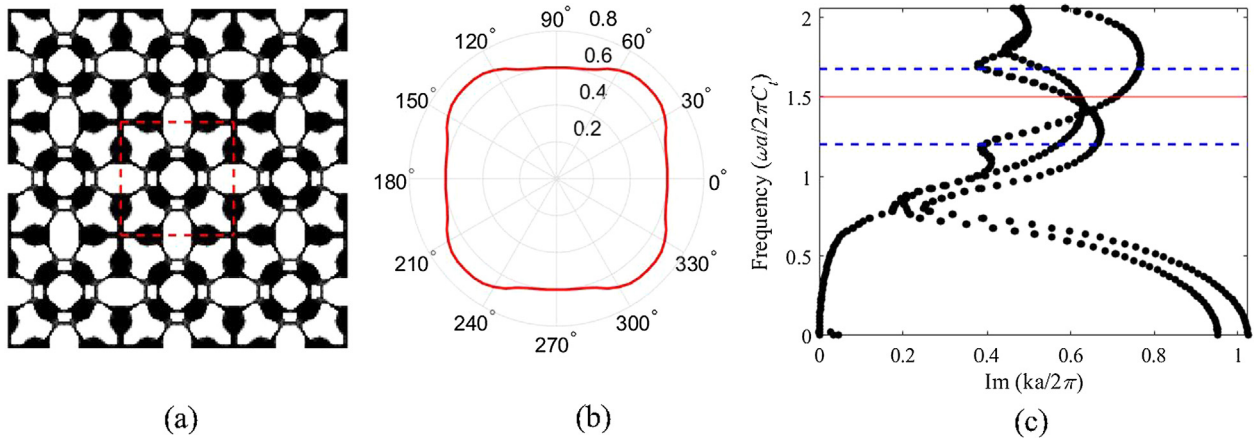

Fig. 9. (a) Optimized topology, (b) equal attenuation factor contour and (c) the imaginary part of complex band diagram for $\theta = 0°$ for out-of-plane waves at frequency $\Omega = 1.5$.

Table 1
The attenuation factor, corresponding angle of incidence and effective bulk modulus of optimized designs for out-of-plane waves at different frequencies.

Specified frequency (Ω)	Attenuation factor	Corresponding angle of incidence	Effective bulk modulus (GPa)
0.7	0.261	25°	9.928
0.9	0.394	25°	9.948
1.1	0.502	20°	9.954
1.3	0.652	45°	9.941
1.5	0.602	0°	10.011

while the stiffness constraint can be added to the objective function by introducing a Lagrangian multiplier. The modified objective function is stated as,

$$\max: f^*(x_i) = \sum_{j=1}^{N} w_j k''_{\theta_j} + \lambda(\kappa^H - \kappa^*) \tag{29}$$

Thus, the sensitivity of the modified objective function is calculated by

$$\frac{\partial f^*(x_i)}{\partial x_i} = \sum_{j=1}^{N} w_j \frac{\partial k''_{\theta_j}}{\partial x_i} + \lambda \frac{\partial \kappa^H}{\partial x_i} \tag{30}$$

When κ^H is equal to κ^*, the above equation is equivalent to the objective function defined in Eq. (26), Otherwise, if $\kappa^H > \kappa^*$, which means the constraint is already satisfied, λ is set to be 0; if $\kappa^H < \kappa^*$, which means the constraint is not satisfied yet, we need to maximize κ^H first, so λ needs to be infinity. Therefore, the Lagrangian multiplier is determined before the calculation of the overall sensitivity of the modified objective function. Here we introduce an intermediate parameter z for the better control of λ as,

$$\lambda = \frac{1-z}{z} \tag{31}$$

where z varies from an extremely small value $z_{\min}$, e.g., 10^{-20}, to 1, so the resulting Lagrangian multiplier λ locates in the range of 0 to infinity.

To find the proper value of z in each iteration during the optimization, we set two bound values of z as $z_{lower} = z_{\min}$ and $z_{upper} = 1$. The program starts from an initial guess $z = 1$ and calculates the sensitivity numbers by Eq. (30). Based on the ranking of the sensitivity numbers, the design variables are updated to satisfy the volume fraction in the next iteration. The homogenized stiffness κ^H in the next iteration, κ^H_{iter+1}, can be estimated with the variation of the design variables as,

$$\kappa^H_{iter+1} = \kappa^H_{iter} + \sum_i \frac{d\kappa^H_{iter}}{dx_i} \Delta x_i \tag{32}$$

Thereafter, if $\kappa^H_{iter+1} < \kappa^*$, which means the constraint is not satisfied, we move the upper bound z_{upper} to z and update z with a smaller value to enlarge the Lagrangian multiplier

$$z = \frac{z + z_{lower}}{2} \tag{33}$$

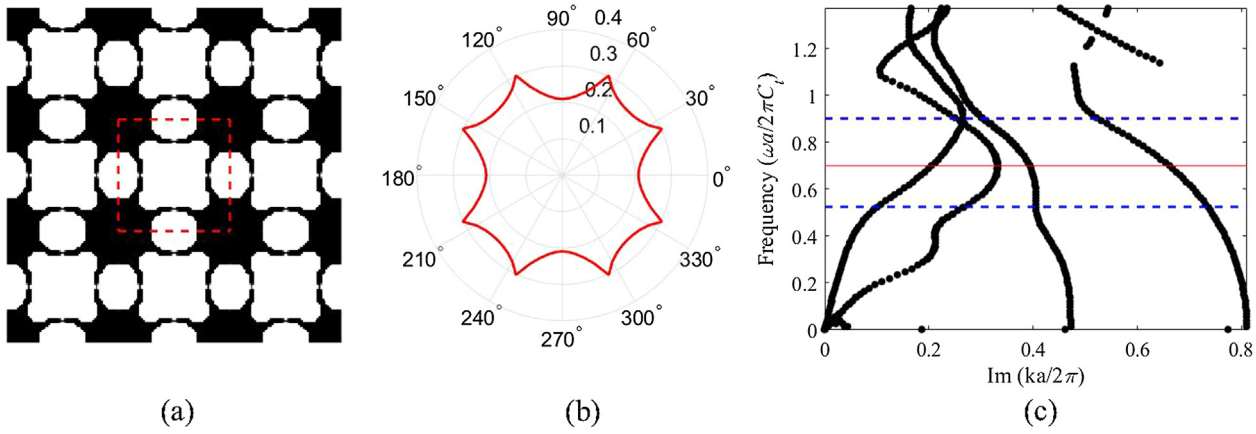

Fig. 10. (a) Optimized topology, (b) equal attenuation factor contour and (c) the imaginary part of complex band diagram for $\theta = 0°$ for in-plane waves at frequency $\Omega = 0.7$.

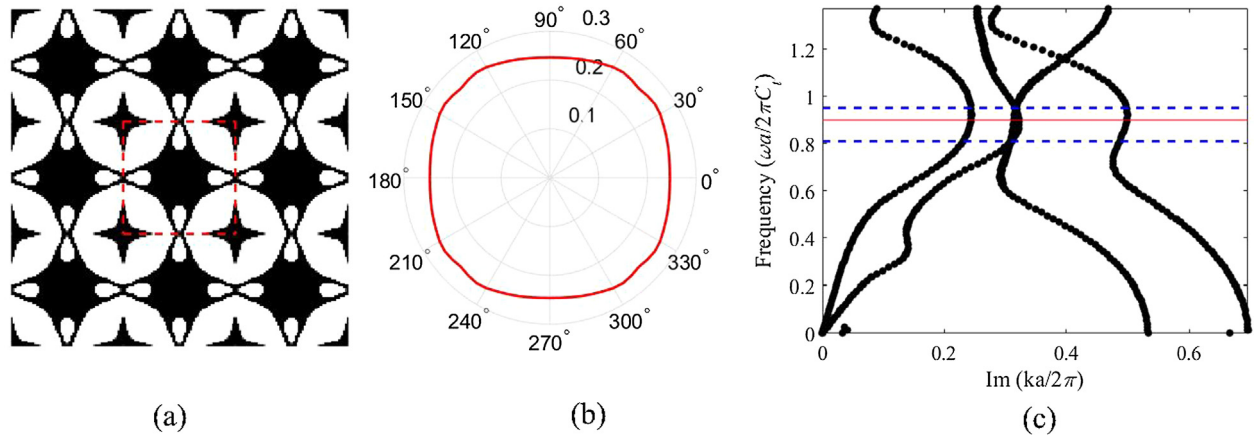

Fig. 11. (a) Optimized topology, (b) equal attenuation factor contour and (c) the imaginary part of complex band diagram for $\theta = 0°$ for in-plane waves at frequency $\Omega = 0.9$.

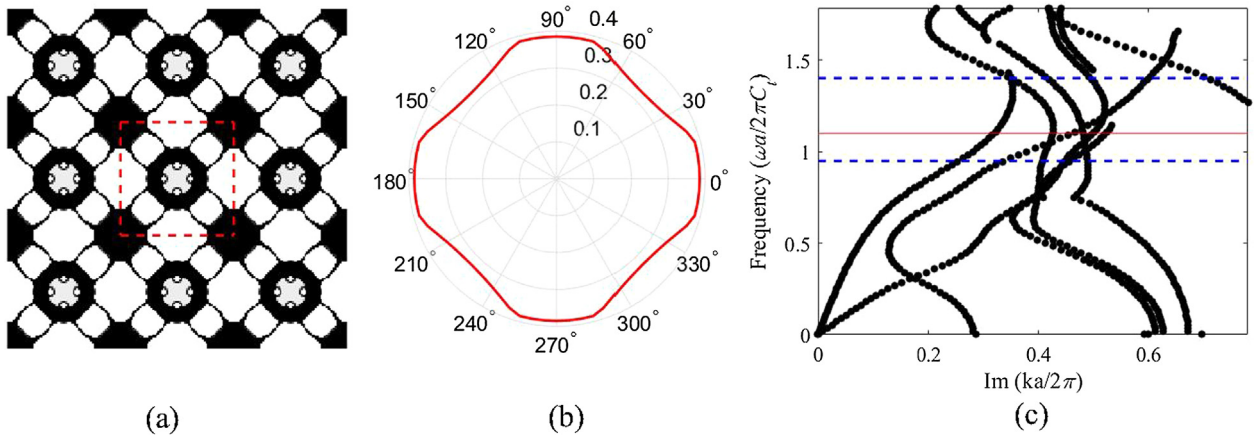

Fig. 12. (a) Optimized topology, (b) equal attenuation factor contour and (c) the imaginary part of complex band diagram for $\theta = 45°$ for in-plane waves at frequency $\Omega = 1.1$.

On the other hand, if $\kappa^H_{iter+1} > \kappa^*$, we move the lower bound z_{lower} to z and update z with a larger value

$$z = \frac{z + z_{upper}}{2} \tag{34}$$

This procedure is repeated until $z_{upper} - z_{lower}$ is less than 10^{-15} and an appropriate Lagrangian multiplier is obtained. It should be noted that the Lagrangian multiplier linearly estimates a proper balance between the attenuation factor and the effective bulk modulus based on the current design as given in Eq. (32). It will be convergent to a constant value after some oscillations.

3.2. BESO procedure

The BESO method was originally proposed for topology optimization of structures [58–60]. In this paper, the BESO method will be

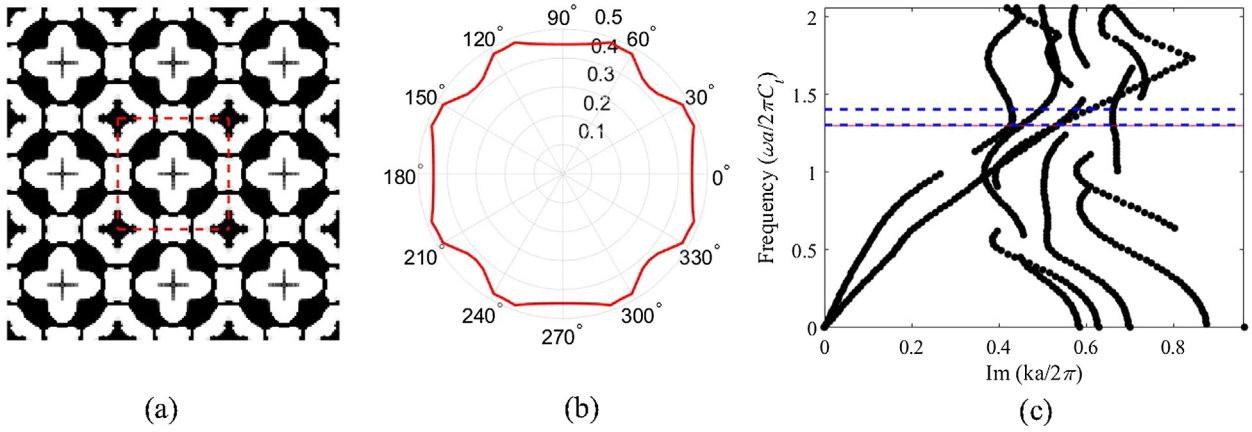

Fig. 13. (a) Optimized topology, (b) equal attenuation factor contour and (c) the imaginary part of complex band diagram for $\theta = 45°$ for in-plane waves at frequency $\Omega = 1.3$.

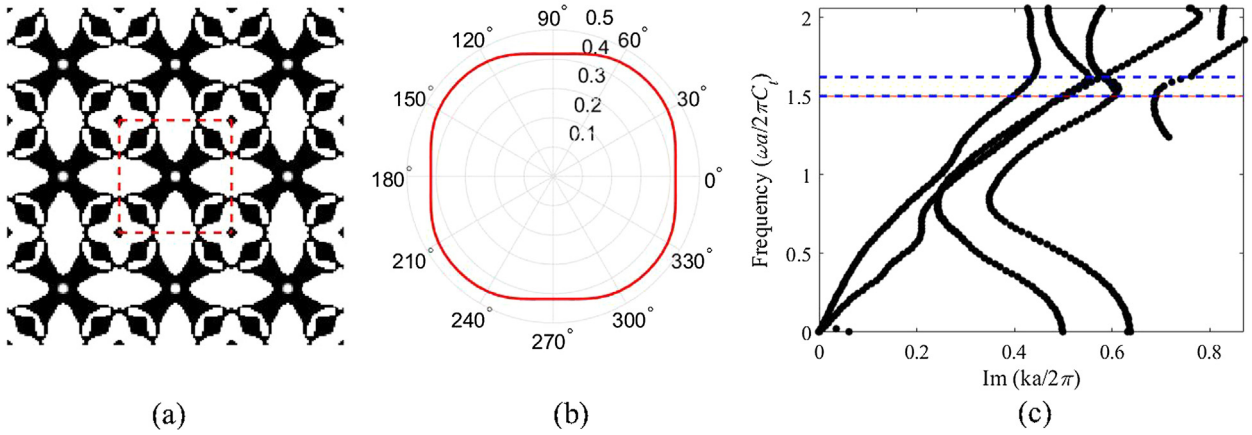

Fig. 14. (a) Optimized topology, (b) equal attenuation factor contour and (c) the imaginary part of complex band diagram for $\theta = 0°$ for in-plane waves at frequency $\Omega = 1.5$.

Table 2
The attenuation factor, corresponding angle of incidence and effective bulk modulus of optimized designs for in-plane waves at different frequencies.

Specified frequency (Ω)	Attenuation factor	Corresponding angle of incidence	Effective bulk modulus (GPa)
0.7	0.209	0°	9.95
0.9	0.246	0°	9.99
1.1	0.328	45°	9.88
1.3	0.423	45°	9.95
1.5	0.418	0°	9.95

extended to maximize the attenuation factor of elastic waves in viscoelastic PCs while satisfying volume and stiffness constraints. At the beginning of each iteration, a target volume fraction of material 2 is determined for updating the design variables by,

$$V_{f,iter+1}^{2} = V_{f,iter}^{2}(1-ER) \text{ when } V_{f,iter+1}^{2} > V_{f}^{2*} \tag{35}$$

where ER is the evolutionary volume ratio. In this paper, BESO starts from an initial design, which is almost full of material 2, and gradually decreases the volume fraction [60,61]. Once the volume constraint V_f^{2*} is satisfied, the volume fraction will be kept as a constant for the remaining iterations.

Then the elemental sensitivity numbers, which indicate the variation of the modified objective function with regard to the change of the elemental design variable, is computed by,

$$\tilde{\alpha}_i^{iter} = \frac{\partial f^*(x_i)}{\partial x_i} \tag{36}$$

Based on the relative ranking of the elemental sensitivities, the threshold of sensitivities is determined by using the bi-section method to satisfy the volume fraction in each iteration. BESO will modify the design variables from 0 to 1 for elements with higher sensitivity numbers than the threshold and from 1 to 0 for elements with lower ones. The update scheme can be summarized as,

$$x_i^{iter+1} = \begin{cases} \min(x_i^{iter} + \Delta x, 1) & if \quad \tilde{\alpha}_i^{iter} > \tilde{\alpha}_{th}^{iter} \\ \max(x_i^{iter} - \Delta x, 0) & if \quad \tilde{\alpha}_i^{iter} < \tilde{\alpha}_{th}^{iter} \end{cases} \tag{37}$$

where $\Delta x = 0.1$ is used throughout the paper. Although discrete intermediate design variables are used during the optimization process, the final design is naturally convergent to an almost 0/1 design as demonstrated in numerical examples.

Topology optimization on continuum structures often encounters numerical instabilities, e.g. checkerboard and mesh-dependency. These numerical instabilities can be avoided by employing a filter scheme, which is also adopted in this study.

The optimization process is briefly outlined as follows

Step 1: Define BESO parameters: volume fraction constraint, evolution rate and filter radius.
Step 2: Construct the initial design and discretize the structure into finite elements.
Step 3: Conduct finite element analysis for viscoelastic PCs and

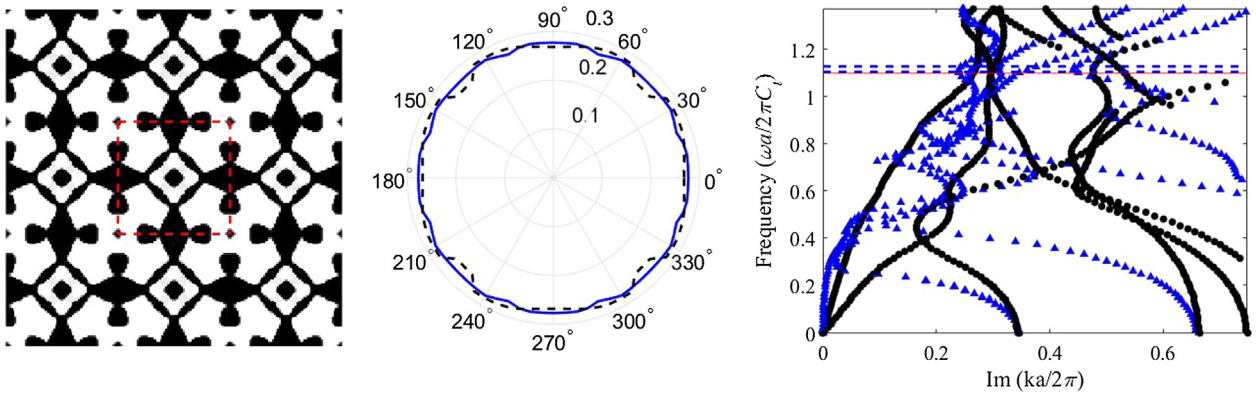

Fig. 15. (a) Optimized topology, (b) equal attenuation factor contours (blue solid line and black dotted line denote out-of-plane and in-plane respectively) and (c) the imaginary part of complex band diagram (the blue triangle points and black circle points denote out-of-plane and in-plane respectively, the blue dotted lines denote upper and bottom bounds of the complete band gap, the red solid line denote the specified frequency) for out-of-plane and in-plane waves at frequency Ω = 1.1. (For interpretation of the references to colour in this figure legend, the reader is referred to the web version of this article.)

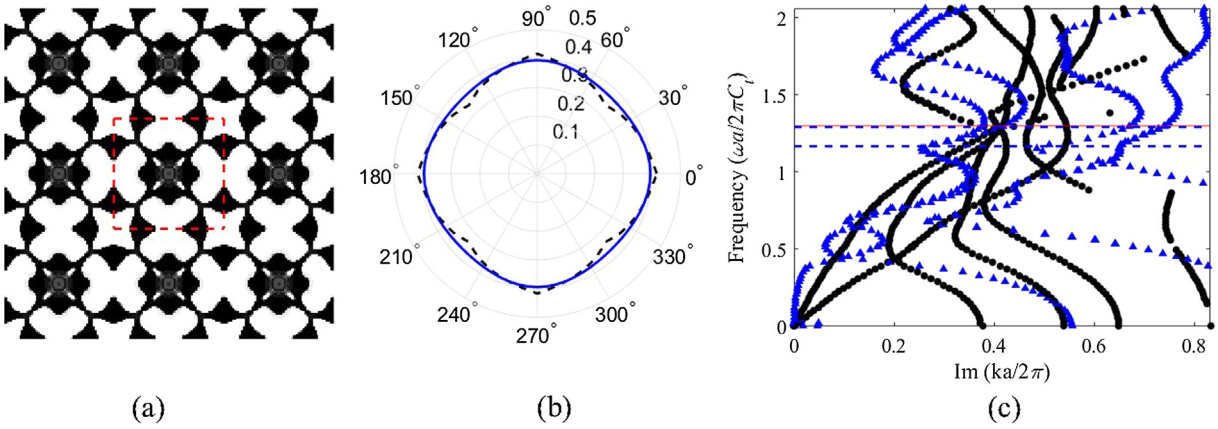

Fig. 16. (a) Optimized topology, (b) equal attenuation factor contours and (c) the imaginary part of complex band diagram for out-of-plane and in-plane waves at frequency Ω = 1.3.

compute attenuation factor and effective bulk modulus according to Eqs. (6) and (9).
Step 4: Determine the target volume fraction of material 2 and current stiffness constraint according to Eqs. (35) and (10).
Step 5: Calculate sensitivity numbers according to Eq. (36).
Step 6: Determine the Lagrangian multiplier according to Eqs. 31–34.
Step 7: Filter the sensitivity numbers.
Step 8: Update design variables according to Eq. (37).
Step 9: Repeat Steps 3–8 until the volume fraction, objective function and topology are stably convergent.

4. Results and discussion

To demonstrate the capability of the proposed BESO algorithm, this section will present a number of optimization results for the out-of-plane mode, in-plane mode and the combined mode of these two. The 2D solid viscoelastic PC in consideration consists of square arrays of pure elastic Au inclusions in a viscoelastic Epoxy matrix. The viscosity of Epoxy is assumed to increase linearly with frequency as is proper to polymers [61]. The physical properties of Epoxy are $\rho_1 = 1200\,\mathrm{kg/m^3}$, $\mu_1^* = 1.61\,\mathrm{GPa} + i\omega\eta_{44}$ and $\lambda_1^* = 6.38\,\mathrm{GPa} + 3.96i\omega\eta_{44}$, where $\eta_{44} = 1000\,\mathrm{Pa}$ denotes the viscosity. The physical properties of Au are $\rho_2 = 19500\,\mathrm{kg/m^3}$, $\mu_2 = 29.93\,\mathrm{GPa}$ and $\lambda_2 = 65.45\,\mathrm{GPa}$. Epoxy and Au are denoted as the white and black in the pictures, respectively. The lattice constant is $a = 1$ cm and the primitive unit cell is discretized into 64×64 linear 4-node elements. For convenience, the frequency is normalized with $\Omega = \omega a/2\pi C_t$ where $C_t = \sqrt{\mathrm{real}(\mu_1^*)/\rho_1}$ denotes the transverse wave speed in matrix, and the wave vector is normalized with $ka/2\pi$. BESO parameters used in most cases are $ER = 0.02$, $V_f^* = 0.4$, $p = 3$, and $r_{\min} = 0.028$ cm.

4.1. Out-of-plane waves

4.1.1. Influence of stiffness constraint

To investigate the influence of stiffness constraint on the optimized attenuation factor and topology, we conduct a series of optimization tests for out-of-plane modes at Ω = 0.9 with the stiffness constraint ratio β varying from 0 to 0.7. It is noted that the optimization tends to maximize the bulk modulus rather than attenuation factor when $\beta > 0.7$, and thus only the results with $\beta \leqslant 0.7$ are presented. The maximized attenuation factor against different constraint ratio β is plotted in Fig. 2 along with the corresponding optimized topologies consisting of 3 × 3 unit cells. The primitive unit cell is given in the red dash box. It can be seen that the optimal attenuation factors and topologies are the same when $\beta \leqslant 0.4$, since the stiffness constraints in these cases are always satisfied during the iterations. That means that the stiffness constraints are inactive in those cases and the optimizations are only to maximize the attenuation factors. The optimized topologies of the unit cell show that the elastic and stiff materials are isolated by the viscoelastic and soft material. The maximized attenuation factor declines continuously when β increases from 0.4 to 0.7. Meanwhile, the stiff and elastic materials in the optimized topologies become connected and the connections become wider when β

increases. In the following examples, β is set as 0.6 to achieve final structures with a relatively large attenuation factor and effective bulk modulus simultaneously.

As an illustrative example, Figs. 3 and 4 present the evolution histories of effective bulk modulus, attenuation factor, volume fraction and the topology for the optimization case with $\Omega = 0.9$ and $\beta = 0.6$. BESO starts from an initial design with volume fraction V_f^2 close to 1 and the effective bulk modulus is almost equal to the HS upper bound value. Fig. 3 shows that the stiffness constraint gradually changes with the volume, which helps to stabilize the optimization process. At the first optimization stage, the effective bulk modulus is greater than the stiffness constraint, which indicates the Lagrangian multiplier is equal to 0. In these iterations, the objective is to maximize the attenuation factor only, and the attenuation factor increases steadily (see Fig. 4). As the volume fraction keeps dropping, the effective bulk modulus approaches to the stiffness constraint that is still decreasing. The Lagrangian multiplier begins to play an important role in the balance of maximizing the attenuation factor or the effective bulk modulus. In these iterations, the attenuation factor experiences a fluctuating period because the modified objective function of the optimization problem changes with the value of the Lagrangian multiplier. Following the procedure illustrated in Section 3.1, the value of the Lagrangian multiplier is determined based on the current design and is updated step by step. During this searching process, the fluctuation of the attenuation factor is inevitable. Once the value of the Lagrangian multiplier is convergent to a constant, such a fluctuation in the attenuation factor naturally will disappear as shown in Fig. 4. The optimization finally converges to a clear 0/1 topology with the maximum attenuation factor under the given volume constraint. The whole optimization takes around 110 iterations, which demonstrates the efficiency of the proposed algorithm.

4.1.2. Out-of-plane results for different specified frequencies

In this section, optimization results with $\beta = 0.6$ at different specified frequencies are presented for out-of-plane modes. Figs. 5–9 show the optimized topologies, equal attenuation factor contours and the imaginary part of complex band diagrams at frequencies $\Omega = 0.7$, 0.9, 1.1, 1.3 and 1.5, respectively. The imaginary parts of complex band diagrams are constructed only for the direction at which the imaginary part of wave vector is minimum. The attenuation factors, corresponding angle of incidence and effective bulk modulus of these optimized designs are given in Table 1. It can be seen that the effective bulk moduli in all cases are approximately equal to the stiffness constraint, $\kappa^* = 9.939$ GPa. It is observed that the stiff material 2 is interconnected in all the optimized topologies to satisfy the stiffness constraint. We also compute the classic band diagrams of the optimized topologies when the viscosity of Epoxy is not considered. There are band gaps appearing around the specified frequencies and their upper and bottom bounds are denoted as blue dotted lines in the complex band diagram. It can be seen that the specified frequencies, denoted as red solid lines, are all located within the band gaps. It means that the attenuation of waves by the viscoelastic PCs is a combination of dispersive and dissipative effects.

4.2. In-plane waves

Maximizing the attenuation factors for in-plane waves is more difficult than that for out-of-plane waves, since both longitudinal and transverse waves are involved. Figs. 10–14 present the resulting optimized topologies, equal attenuation factor contours and the imaginary part of complex band diagrams at frequencies $\Omega = 0.7$, 0.9, 1.1, 1.3 1.5. None of these topologies has been reported yet. Table 2 summarizes the attenuation factor, corresponding angle of incidence and effective bulk modulus of these optimized designs. It is noticed that all the attenuation factors are smaller than those for out-of plane waves. The effective bulk modulus of these optimized designs are also approximately equal to the bulk modulus constraint. Similar to the optimization of out-of-plane waves, band gaps emerge around the specified frequencies when the viscosity of material is neglected and the target frequencies to attenuate are also located within the band gaps.

4.3. Out-of-plane and in-plane waves

This section is try to maximize the attenuation factors for both out-of-plane and in-plane waves. Figs. 15–16 present the resulting optimized topologies, equal attenuation factor contours and the imaginary part of complex band diagrams at frequencies $\Omega = 1.1$ and 1.3. The attenuation factors of the out-of-plane wave vectors are 0.269 and 0.369 at $\Omega = 1.1$ and 1.3, respectively. The corresponding incident angles are $\theta = 45°$ and 20°. For in-plane waves, the attenuation factors under those specified frequencies are respectively 0.258 and 0.337, and the corresponding angles are 45. The effective bulk modulus of these optimized designs are all 9.95 GPa. Similar to the optimization of out-of-plane and in-plane waves, complete band gaps occur near the target frequencies when the viscosity is neglected, the specified frequencies are close to the bounds of the complete band gaps.

5. Conclusion

In this paper, we applied the BESO algorithm for the optimal design of 2D viscoelastic PCs. The resulting viscoelastic PCs have the maximum attenuation property of elastic waves at the specified frequencies, and meanwhile possess a prescribed stiffness. The optimization problem has been formulated to maximize the attenuation factor, which is characterized by the minimum of the imaginary part of wave vectors in all directions, subject to the bulk modulus and volume constraints. Based on the sensitivity analysis, BESO gradually adjusts the material distribution within the primitive unit cell, and enlarges the attenuation factor. Numerical examples demonstrate the effectiveness of the proposed BESO method for designing viscoelastic PCs. Various topological patterns of viscoelastic PCs have been obtained for propagating out-of-plane, in-plane and combined out-of-plane and in-plane evanescent waves. Numerical results also indicate that the specified frequencies with high attenuation factors are located in the classic band gap of the optimized topologies when the viscosity is neglected. The fact reveals that the wave attenuation of the optimized viscoelastic PCs attributes to the combined dispersive and dissipative effects. Further research on topology optimization of 3D viscoelastic PCs is recommended.

Acknowledgements

The authors wish to acknowledge the financial support from the Australian Research Council (FT130101094) and State Key Program of National Natural Science of China (61232014).

Appendix A. Supplementary material

Supplementary data associated with this article can be found, in the online version, at https://doi.org/10.1016/j.ultras.2018.05.005.

References

[1] M.H. Lu, L. Feng, Y.F. Chen, Phononic crystals and acoustic metamaterials, Mater. Today 12 (2009) 34–42.
[2] J. Sánchez-Pérez, D. Caballero, R. Martinez-Sala, C. Rubio, J. Sánchez-Dehesa, F. Meseguer, et al., Sound attenuation by a two-dimensional array of rigid cylinders, Phys. Rev. Lett. 80 (1998) 5325.
[3] J. Sánchez-Dehesa, V.M. Garcia-Chocano, D. Torrent, F. Cervera, S. Cabrera, F. Simon, Noise control by sonic crystal barriers made of recycled materials, J. Acoust. Soc. Am. 129 (2011) 1173–1183.
[4] H. Policarpo, M. Neves, A. Ribeiro, Dynamical response of a multi-laminated periodic bar: analytical, numerical and experimental study, Shock Vib. 17 (2010) 521–535.
[5] M.I. Hussein, G.M. Hulbert, R.A. Scott, Dispersive elastodynamics of 1D banded

materials and structures: design, J. Sound Vib. 307 (2007) 865–893.
[6] M. Sigalas, Elastic wave band gaps and defect states in two-dimensional composites, J. Acoust. Soc. Am. 101 (1997) 1256–1261.
[7] M. Sigalas, Defect states of acoustic waves in a two-dimensional lattice of solid cylinders, J. Appl. Phys. 84 (1998) 3026–3030.
[8] M. Torres, F.M. de Espinosa, D. Garcia-Pablos, N. Garcia, Sonic band gaps in finite elastic media: surface states and localization phenomena in linear and point defects, Phys. Rev. Lett. 82 (1999) 3054.
[9] R. Lucklum, M. Ke, M. Zubtsov, Two-dimensional phononic crystal sensor based on a cavity mode, Sens. Actuators, B 171 (2012) 271–277.
[10] M. Kafesaki, M. Sigalas, N. Garcia, Frequency modulation in the transmittivity of wave guides in elastic-wave band-gap materials, Phys. Rev. Lett. 85 (2000) 4044.
[11] Y. Pennec, B. Djafari-Rouhani, J. Vasseur, A. Khelif, P. Deymier, Tunable filtering and demultiplexing in phononic crystals with hollow cylinders, Phys. Rev. E 69 (2004) 046608.
[12] S. Mohammadi, A. Adibi, On chip complex signal processing devices using coupled phononic crystal slab resonators and waveguides, AIP Adv. 1 (2011) 041903.
[13] Y. Pennec, J.O. Vasseur, B. Djafari-Rouhani, L. Dobrzyński, P.A. Deymier, Two-dimensional phononic crystals: examples and applications, Surf. Sci. Rep. 65 (2010) 229–291.
[14] A. Khelif, B. Djafari-Rouhani, J. Vasseur, P.A. Deymier, Transmission and dispersion relations of perfect and defect-containing waveguide structures in phononic band gap materials, Phys. Rev. B 68 (2003) 024302.
[15] A. Khelif, A. Choujaa, S. Benchabane, B. Djafari-Rouhani, V. Laude, Guiding and bending of acoustic waves in highly confined phononic crystal waveguides, Appl. Phys. Lett. 84 (2004) 4400–4402.
[16] J. Vasseur, P.A. Deymier, B. Djafari-Rouhani, Y. Pennec, A. Hladky-Hennion, Absolute forbidden bands and waveguiding in two-dimensional phononic crystal plates, Phys. Rev. B 77 (2008) 085415.
[17] Y.F. Li, F. Meng, S. Zhou, M.-H. Lu, X. Huang, Broadband all-angle negative refraction by optimized phononic crystals, Sci. Rep. 7 (2017).
[18] Y. Chen, F. Meng, G. Sun, G. Li, X. Huang, Topological design of phononic crystals for unidirectional acoustic transmission, J. Sound Vib. 410 (2017) 103–123.
[19] J.D. Ferry, Viscoelastic Properties of Polymers, John Wiley & Sons, 1980.
[20] H.A. Ba'Ba'A, M. Nouh, An investigation of vibrational power flow in one-dimensional dissipative phononic structures, J. Vib. Acoust. 139 (2017).
[21] M.J. Frazier, M.I. Hussein, Generalized Bloch's theorem for viscous metamaterials: dispersion and effective properties based on frequencies and wavenumbers that are simultaneously complex, C. R. – Phys. 17 (2016) 565–577.
[22] M.J. Frazier, M.I. Hussein, Viscous-to-viscoelastic transition in phononic crystal and metamaterial band structures, J. Acoust. Soc. Am. 138 (2015) 3169–3180.
[23] Y. Ma, F. Scarpa, D. Zhang, B. Zhu, L. Chen, J. Hong, A nonlinear auxetic structural vibration damper with metal rubber particles, Smart Mater. Struct. 22 (2013) 084012.
[24] R.P. Moiseyenko, V. Laude, Material loss influence on the complex band structure and group velocity in phononic crystals, Phys. Rev. B 83 (2011) 064301.
[25] V. Laude, J.M. Escalante, A. Martínez, Effect of loss on the dispersion relation of photonic and phononic crystals, Phys. Rev. B 88 (2013) 224302.
[26] J. Hwan Oh, Y. Jae Kim, Y. Young Kim, Wave attenuation and dissipation mechanisms in viscoelastic phononic crystals, J. Appl. Phy. 113 (10) (2013) 212301.
[27] J.M. Manimala, C. Sun, Microstructural design studies for locally dissipative acoustic metamaterials, J. Appl. Phys. 115 (2014) 023518.
[28] Y.F. Wang, Y.S. Wang, V. Laude, Wave propagation in two-dimensional viscoelastic metamaterials, Phys. Rev. B 92 (2015) 104110.
[29] A. Krushynska, V. Kouznetsova, M. Geers, Visco-elastic effects on wave dispersion in three-phase acoustic metamaterials, J. Mech. Phys. Solids 96 (2016) 29–47.
[30] E. Andreassen, J.S. Jensen, Analysis of phononic bandgap structures with dissipation, J. Vib. Acoust. 135 (2013) 041015.
[31] M.A. Nouh, O.J. Aldraihem, A. Baz, Periodic metamaterial plates with smart tunable local resonators, J. Intell. Mater. Syst. Struct. (2015).
[32] A.S. Phani, M.I. Hussein, Analysis of damped Bloch waves by the Rayleigh perturbation method, J. Vib. Acoust. 135 (2013) 041014.
[33] M.I. Hussein, M.J. Frazier, Band structure of phononic crystals with general damping, J. Appl. Phys. 108 (2010) 093506.
[34] M.I. Hussein, Theory of damped Bloch waves in elastic media, Phys. Rev. B 80 (2009) 212301.
[35] Y.P. Zhao, P.J. Wei, The band gap of 1D viscoelastic phononic crystal, Comput. Mater. Sci. 46 (2009) 603–606.
[36] V. Laude, Y. Achaoui, S. Benchabane, A. Khelif, Evanescent Bloch waves and the complex band structure of phononic crystals, Phys. Rev. B 80 (2009) 092301.
[37] V. Romero-García, J.V. Sánchez-Pérez, S. Castiñeira-Ibáñez, L. Garcia-Raffi, Evidences of evanescent Bloch waves in phononic crystals, Appl. Phys. Lett. 96 (2010) 124102.
[38] G.L. Yi, B.D. Youn, A comprehensive survey on topology optimization of phononic crystals, Struct. Multidiscip. Optim. (2016) 1–30.
[39] O. Sigmund, J.S. Jensen, Systematic design of phononic band–gap materials and structures by topology optimization, Philos. Trans. R. Soc. London, A 361 (2003) 1001–1019.
[40] G.A. Gazonas, D.S. Weile, R. Wildman, A. Mohan, Genetic algorithm optimization of phononic bandgap structures, Int. J. Solids Struct. 43 (2006) 5851–5866.
[41] O.R. Bilal, M.I. Hussein, Optimization of phononic crystals for the simultaneous attenuation of out-of-plane and in-plane waves, ASME 2011 International Mechanical Engineering Congress and Exposition, American Society of Mechanical Engineers, 2011, pp. 969–972.
[42] O.R. Bilal, M.I. Hussein, Ultrawide phononic band gap for combined in-plane and out-of-plane waves, Phys. Rev. E 84 (2011) 065701.
[43] H.W. Dong, X.X. Su, Y.S. Wang, Multi-objective optimization of two-dimensional porous phononic crystals, J. Phys. D Appl. Phys. 47 (2014) 155301.
[44] Z.F. Liu, B. Wu, C.F. He, Band-gap optimization of two-dimensional phononic crystals based on genetic algorithm and FPWE, Waves Random Complex Medium 24 (2014) 286–305.
[45] C.J. Rupp, A. Evgrafov, K. Maute, M.L. Dunn, Design of phononic materials/structures for surface wave devices using topology optimization, Struct. Multidiscip. Optim. 34 (2007) 111–121.
[46] H.W. Dong, X.X. Su, Y.S. Wang, C.Z. Zhang, Topological optimization of two-dimensional phononic crystals based on the finite element method and genetic algorithm, Struct. Multidiscip. Optim. 50 (2014) 593–604.
[47] Y.F. Li, X. Huang, F. Meng, S. Zhou, Evolutionary topological design for phononic band gap crystals, Struct. Multidiscip. Optim. (2016) 1–23.
[48] Y.F. Li, X. Huang, S. Zhou, Topological design of cellular phononic band gap crystals, Materials 9 (2016) 186.
[49] L. D'Alessandro, B. Bahr, L. Daniel, D. Weinstein, R. Ardito, Shape optimization of solid-air porous phononic crystal slabs with widest full 3D bandgap for in-plane acoustic waves, J. Comput. Phys. 344 (2017) 465–484.
[50] Y. Chen, X. Huang, G. Sun, X. Yan, G. Li, Maximizing spatial decay of evanescent waves in phononic crystals by topology optimization, Comput. Struct. 182 (2017) 430–447.
[51] X. Huang, S. Zhou, G. Sun, G. Li, Y.M. Xie, Topology optimization for microstructures of viscoelastic composite materials, Comput. Methods Appl. Mech. Eng. 283 (2015) 503–516.
[52] E. Andreassen, J.S. Jensen, Topology optimization of periodic microstructures for enhanced dynamic properties of viscoelastic composite materials, Struct. Multidiscip. Optim. 49 (2014) 695–705.
[53] C. Kittel, D.F. Holcomb, Introduction to solid state physics, Am. J. Phys. 35 (1967) 547–548.
[54] M.P. Bendsøe, N. Kikuchi, Generating optimal topologies in structural design using a homogenization method, Comput. Methods Appl. Mech. Eng. 71 (1988) 197–224.
[55] O. Sigmund, Tailoring materials with prescribed elastic properties, Mech. Mater. 20 (1995) 351–368.
[56] Z. Hashin, S. Shtrikman, A variational approach to the theory of the elastic behaviour of multiphase materials, J. Mech. Phys. Solids 11 (1963) 127–140.
[57] V. Komkov, K.K. Choi, E.J. Haug, Design Sensitivity Analysis of Structural Systems, Academic press, 1986.
[58] X. Huang, Y.M. Xie, Convergent and mesh-independent solutions for the bi-directional evolutionary structural optimization method, Finite Elem. Anal. Des. 43 (2007) 1039–1049.
[59] X. Huang, Y.M. Xie, Bi-directional evolutionary topology optimization of continuum structures with one or multiple materials, Comput. Mech. 43 (2009) 393–401.
[60] X. Huang, Y.M. Xie, Evolutionary Topology Optimization of Continuum Structures: Methods and Applications, John Wiley & Sons, 2010.
[61] B.A. Auld, Acoustic Fields and Waves in Solids, Рипол Классик, 1973.